Nanoscale

PAPER

View Article Online
View Journal

Cite this: DOI: 10.1039/d5nr03611a

Atmospheric pressure plasma synthesis of monophase bismuth nanocrystals

Ali Khatibi, *[a,b] Miryam Arredondo,[c] Paul Maguire †[a] and Davide Mariotti *[d]

Nanostructured single-phase metal crystals with single and well-defined crystal structures exhibit unique, predictable, and stable properties that are distinct from those of multiphase crystals. However, synthesizing such pure nanocrystals is challenging, as bismuth exhibits multiple polymorphs and crystal phases that often prevent achieving monophase crystals, especially under atmospheric pressure. In this study, we present a gas-phase synthesis method using non-equilibrium plasma to produce high-purity, monophase bismuth nanocrystals (BiNCs) at atmospheric pressure. This approach employs a solid bismuth precursor, eliminating the need for hazardous solvents and offering a safer, more environmentally friendly alternative. By controlling plasma absorbed power and incorporating hydrogen to the process gas, localized melting and surface nucleation are promoted, resulting in the formation of BiNCs with a rhombohedral crystal phase. High-resolution transmission electron microscopy, X-ray diffraction and Raman spectroscopy confirmed the crystallinity of the BiNCs, exhibiting sharp faceting in some cases. X-ray photoelectron spectroscopy and energy-dispersive X-ray spectroscopy revealed that the nanocrystals were predominantly composed of elemental bismuth with minimal surface oxidation when exposed to the atmosphere.

Received 26th August 2025,
Accepted 26th November 2025

DOI: 10.1039/d5nr03611a

rsc.li/nanoscale

1. Introduction

Mono-elemental metal nanocrystals represent a vital class of materials whose properties differ significantly from their bulk counterparts[1,2] due to their strong influence of their reduced size and surface effects. These nanoscale phenomena make them crucial for applications in electronics, catalysis and energy storage.[1,2] Among these, bismuth nanocrystals (BiNCs) have distinctive physical and chemical properties that contrast sharply from those of bulk bismuth. While bulk bismuth is a semi-metal with low electrical conductivity and high thermal conductivity, BiNCs exhibit size-dependent behaviors,[3,4] such as quantum confinement effects and enhanced catalytic activity. These features enable applications in fields like thermoelectric energy conversion, plasmonic devices and electrochemical catalysis.[5–7]

Bismuth naturally exhibits multiple polymorphs and crystal phases, with the rhombohedral phase being the most stable.[8,9] However, synthesizing BiNCs with a pure rhombohedral phase remains challenging due to bismuth's tendency to form several polymorphs under varying synthesis conditions.[10–12] Polymorphism is greatly influenced by temperature,[12] chemical environment and other factors during synthesis,[13] often leading to mixed-phase products that compromise material performance.[14,15] Solution-based synthesis methods, such as hydrothermal techniques,[16] require precise control over reaction conditions to favor the formation of the desired phase and typically involve the use of hazardous metal–organic precursors, solvents and additives, which influence the nucleation and growth processes. Such chemicals are not only expensive but also pose significant environmental and safety concerns. Furthermore, such processes often necessitate additional purification steps to remove by-products, lowering yields and adding complexity to the overall process.[5–7,13,16] The toxic waste generated from solvents and additives highlights the need for safer and more sustainable methods. Addressing the limitations of current synthesis techniques is essential for the reliable production of monophase BiNCs. The development of alternative methods that avoid hazardous chemicals and eliminate complex purification steps would simplify the synthesis and improve scalability, making BiNCs production more accessible for industrial-scale applications in various technological fields. Low-pressure synthesis techniques utilizing solid precursors, such as vapour deposition,[12,17–20] pulse laser deposition[21] and molecular beam epitaxy[22,23] have demonstrated significant promise in producing Bi nanostructures. However, in most cases, these techniques have produced multiphase and polycrystalline bismuth structures.[12,18–20] Furthermore, these methods require high-vacuum environments, which add operational challenges and costs.

[a]School of Engineering, Ulster University, Belfast, UK
[b]Diamond Light Source Ltd., Harwell Science and Innovation Campus, Didcot, UK. E-mail: ali.khatibi@diamond.ac.uk
[c]School of Mathematics and Physics, Queen's University Belfast, Belfast, UK
[d]Department of Design, Manufacturing & Engineering Management, University of Strathclyde, Glasgow, UK. E-mail: davide.mariotti@strath.ac.uk
† Current address: School of Physics & Astronomy, University of Glasgow, UK.

In this study, we present a gas-phase synthesis technique using non-equilibrium atmospheric pressure plasma to produce monophase BiNCs. Our approach uses a solid bismuth precursor in a plasma environment, eliminating the need for hazardous chemicals and complex purification processes. The process exploits plasma's ability to induce localized melting and controlled crystallization at the surface of the sacrificial metal wire electrode. This method not only simplifies the experimental setup but also enables the rapid synthesis of highly crystalline, monophase BiNCs under atmospheric pressure. Our results confirm the formation of BiNCs with rhombohedral structure and some faceted morphologies with high purity. Additionally, we propose a mechanism for BiNCs formation, driven by plasma-induced localized melting and subsequent nucleation under non-equilibrium conditions. Our approach addresses key limitations of existing synthesis methods and offers insights into the development of a plasma-based process for a sustainable pathway for producing high purity monophase metal nanocrystals.

2. Experimental section

2.1. Gas-phase atmospheric pressure plasma synthesis process

The plasma reactor consists of a hollow borosilicate glass capillary (60 mm long) with an internal and external diameter of 3 mm and 4 mm, respectively (Fig. 1). Two parallel rectangular copper electrodes, each 1 mm thick and separated by a 2 mm gap, are fixed around the borosilicate glass capillary by a Perspex frame. A bismuth (Bi) wire (0.9 mm diameter, Fine Metal Ltd), used as a solid precursor which typically contains a native oxide layer on its surface. Before synthesis, the wire is cleaned with isopropyl alcohol and dried using flowing N_2 and then inserted into the glass capillary with one end positioned between the copper electrodes. A 13.56 MHz radio frequency (RF) power is applied to the copper electrodes (as power electrodes), while the bismuth wire is grounded. To sustain the plasma, the applied power is varied from 35 W to 50 W, corresponding to an absorbed plasma power range of 2.0 W to 4.7 W. The plasma absorbed power is measured using an in-line RF VI probe (Impedance Octiv Suite, see also Fig. S1). With increasing plasma absorbed power, the gas discharge first appeared filamentary and then turned into a homogeneous glow discharge (Fig. 1b). The plasma is first ignited by applying a high-voltage pulse to a trigger electrode (a coiled copper wire seen in Fig. 1a and b) placed downstream close to the end of the capillary.

Helium with 1% H_2 is used as the process gas with a constant flow rate of 1 standard litre per minute (sLm). Hydrogen initially acts as a cleaning agent, removing organic impurities and contaminants as well as native oxide from the surface of the Bi wire. Subsequently, hydrogen contributes to increasing the NC production rate. A Perspex frame provides mechanical support and keeps the vertical and radial position of the wire fixed to the frame.

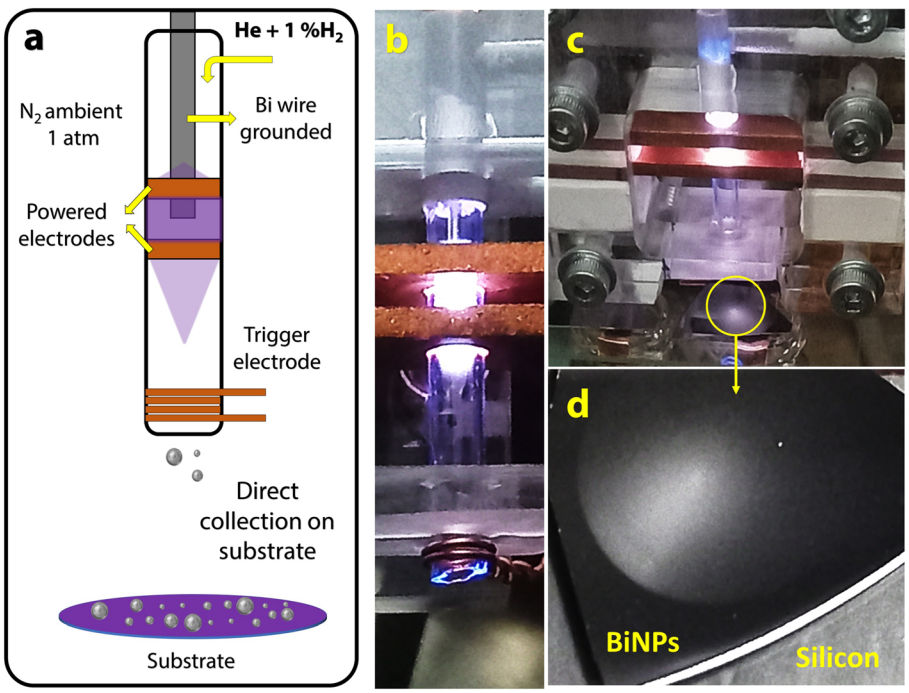

Fig. 1 Atmospheric pressure plasma synthesis. (a) Schematic of plasma reactor setup in an N_2-filled chamber. A Bismuth wire (1 mm in diameter) is inserted into the borosilicate glass tube, with one end grounded and the other end positioned between two copper electrodes. (b and c) A photograph of the non-equilibrium plasma between Bi wire (grounded) and copper electrodes (powered). (d) A photograph of the silicon substrate where BiNCs are deposited.

To reduce the presence of oxygen or moisture in the synthesis process, the plasma reactor is held inside a stainless-steel chamber. Before synthesis, the chamber is evacuated and then filled with pure N_2 gas under atmospheric pressure, which effectively prevents bismuth oxidation during the synthesis process. Each synthesis was carried out for 15 min and BiNCs were collected downstream on a substrate placed 0.8 cm below the capillary end (Fig. 1c and d).

2.2. Materials characterization

Samples for scanning electron microscopy (SEM) analysis were mounted and grounded using double-sided copper tape, on silicon substrates attached to the SEM sample stubs. SEM analysis was carried out using a Hitachi SU5000 equipped with a Schottky field emission source and an Oxford Instruments X-MaxN 80 silicon drift detector, at 5 kV. High-angle annular dark field scanning transmission electron microscopy (HAADF-STEM) and energy dispersive X-ray spectroscopy (EDX) were acquired with a Thermo Fisher Talos F200-X operated at 200 kV equipped with a four-detector in-column Super X spectrometer at an angle of 0.9sr, images were acquired with a dwell time of 8 ms and a pixel size of ~0.13 nm. For these measurements, BiNCs were directly deposited onto holey carbon grids (Agar Scientific) during synthesis, held at 0.8 cm from the capillary exit. This direct deposition method ensured a low-density distribution of nanocrystals across the grid, facilitating single-particle STEM analysis. Raman spectroscopy was employed to obtain the electronic and vibrational properties of the synthesized BiNCs. For this, BiNCs were initially deposited on a silicon substrate, and then placed under the objective of a Horiba Labram 300 Raman spectrometer. A 532 nm laser was used as the excitation source for the Raman measurements. X-ray diffraction (XRD) was performed to determine the crystalline nature of BiNCs using a Malvern Panalytical Empyrean-3, operated in reflection mode at 45 kV and 40 mA, utilizing Cu Kα radiation (λ = 1.54 Å). X-ray photoelectron spectroscopy (XPS) was employed to investigate the surface oxidation of the BiNCs. Samples for both XRD and XPS were prepared and deposited on silicon substrates. For XPS analysis, samples were transferred directly from the nitrogen-filled synthesis chamber to the XPS load chamber under vacuum conditions to minimize exposure to air. XPS analysis was carried out using an ESCALAB XI+ spectrometer (ThermoFisher) equipped with an Al Kα X-ray source (1486 eV) and a spot size of 650 μm. The sample chamber was maintained at a pressure of 10^{-8} bar throughout the measurement process, using an operating current of 10 mA and a voltage of 15 kV. Specific region scans were performed with a resolution of 0.1 eV and a pass energy of 20 eV. The obtained spectra were calibrated using the C 1s peak at 284.8 eV. To remove the native oxide layer from the BiNCs surface, XPS sputter cleaning was performed using a monoatomic argon ion gun set to 2000 eV at a 30° angle, covering a 1.5 mm^2 area on the sample surface.

3. Results and discussion

3.1. Synthesis of BiNCs and analysis of the sacrificial Bi wire electrode

Fig. 2 presents secondary electron (SE) SEM images of BiNCs on a silicon substrate after a 15-minute synthesis (Fig. 2a), as well as the sacrificial Bi wire electrode after synthesis (Fig. 2b and c). At an absorbed plasma power of 2 W, no synthesis and no deposition of Bi NCs was observed on the silicon substrate (Fig. 2a). However, the Bi wire tip exhibited surface roughening, as seen in Fig. 2b and c. As the absorbed power was increased, noticeable changes occurred in the shape of the Bi wire tip. At 3.5 W, the wire tip began to change shape and eventually developed a pronounced "bulge" (Fig. 2b). The deformation of the wire shape is a clear indication of an increase in temperature which is sufficient to cause initial localized surface melting of the Bi wire (Fig. 2b, 3.5 W), followed by extensive re-shaping beyond the tip surface (Fig. 2b, "bulge" at 4.2–4.7 W), suggesting that the degree of deformation and possibly melting is directly related to the power used.

SEM images of the wire surface (Fig. 2c) revealed the presence of Bi particles that had formed directly on the surface of the wire, exhibiting broad size distribution, ranging from as small as ~10 nm to several micrometers in diameter. Notably, irrespective of their sizes, at an absorbed power of 3.5 W, the Bi particles collected on the silicon substrate visibly displayed faceted morphologies, unlike those synthesized at higher powers (4.2–4.7 W), compare Fig. 2a at 3.5 W with 4.2–47 W and Fig. S3a–S4 with Fig. S3b and c. In contrast, at higher absorbed powers, the Bi particles appeared smoother and more spherical (Fig. 2a at 4.2 W and 4.7 W, see also Fig. S3b and c).[13,20] At powers higher than 4.7 W, the plasma became unstable, leading to significant contractions of the Bi wire, pulling away from the plasma, which resulted in the extinction of the plasma and the end of BiNCs formation. While synthesis of BiNCs was possible up to 4.7 W, under these conditions, the optimal operational parameters for the synthesis of BiNCs were determined to be at 3.5 W. It should be noted that, in addition to power, other process parameters can also play a role in shaping the synthesis outcome and, by extension, the properties of BiNCs. However, certain parameters may exhibit lower sensitivity, leading to minimal or negligible variations in the nanocrystal synthesis. The similarity between the particles collected on the substrate (Fig. 2a) and those observed on the wire surface (Fig. 2c) strongly suggests that the formation of BiNCs primarily occurs at the wire surface rather than in the gas phase. This indicates that the wire surface acts as the primary site for nucleation and growth, with the particles subsequently detaching and depositing onto the substrate. This may be specific of this synthesis method, with the Bi wire and under these conditions, as using other metallic sacrificial electrodes or other plasma conditions, the formation of nanoparticles in the gas-phase is also possible and has been observed.[24–27]

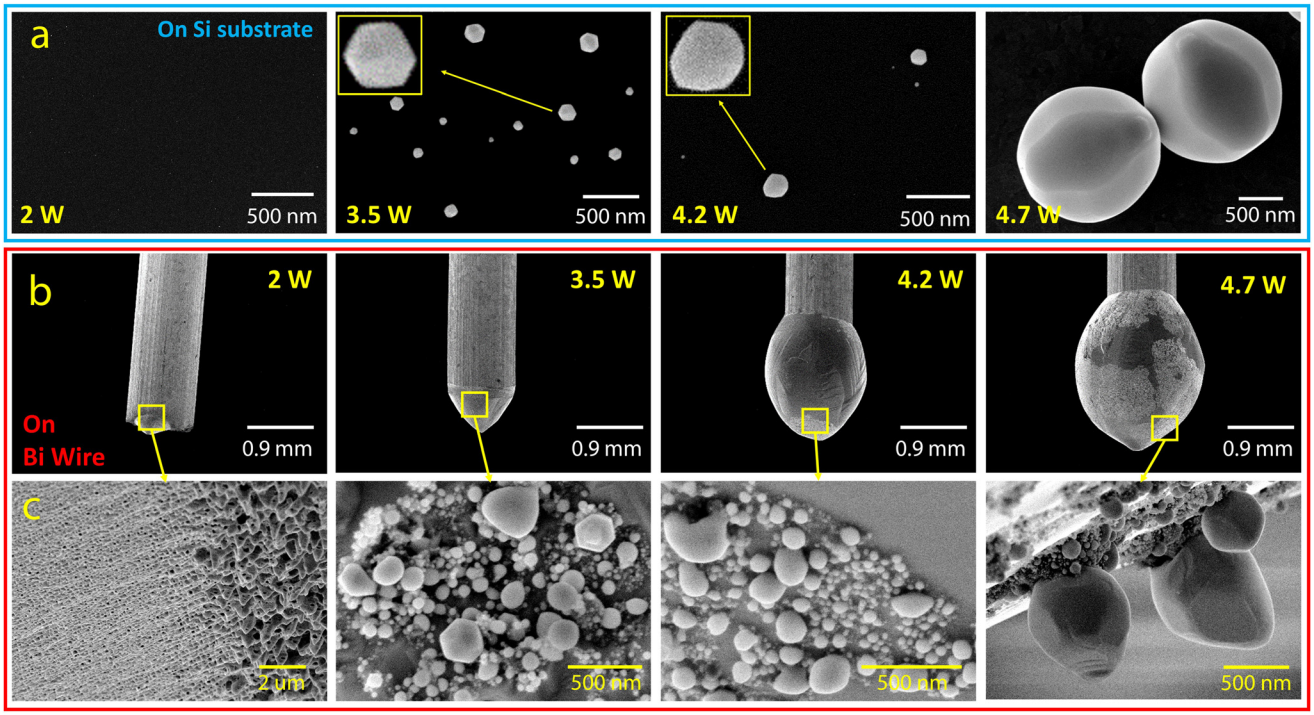

Fig. 2 SE SEM images of (a) BiNCs collected on silicon substrates and the tip of the sacrificial Bi wire electrode (b) imaged at low magnification; and (c) higher magnification images of the wire surface at the locations indicated by yellow squares in (b).

3.2. Analysis of Bi NCs synthesized at 3.5 W

BiNCs synthesized at 3.5 W were selected for further detailed analysis, in part due to their facetted nature (observed to appear more frequently than at under other conditions, Fig. 2, S3 and S4), and favourable synthesis conditions, characterized by its low-energy synthesis conditions and limited wire melting and reshaping. The most stable crystal phase of bismuth is the rhombohedral $R\bar{3}m$ (166) space group, with lattice constants of a = 4.537 Å and c = 11.838 Å,[28,29] as illustrated in Fig. 3a and b. The equilibrium morphology of BiNCs, known as the Wulff shape (Fig. 3c), closely resembles the morphology of the BiNCs deposited on the silicon substrate at an absorbed power of 3.5 W (Fig. 2a) and further shown in Fig. 3d. According to Wulff's construction, the crystal adopts a shape that minimizes their surface energy, resulting in flat, intersecting surfaces at well-defined angles, forming facets, as seen in Fig. 3d and c. The presence of such well-defined facets indicates that the plasma induced crystal growth process enabled balanced growth rates along different crystallographic directions. The relative sizes and orientations of the BiNCs' facets are determined by the crystal's internal structure and the surface energies associated with each crystallographic plane. This balance of surface energies leads to the formation of monophase BiNCs with a consistent rhombohedral structure. To further investigate the crystallinity and structure of the BiNCs, high-angle annular dark-field scanning transmission electron microscopy (HAADF-STEM) was employed. Fig. 3e–g display representative HAADF-STEM images of three different BiNCs, synthesized at 3.5 W, with their corresponding fast Fourier transforms (FFTs) as insets (see Fig. S5 for higher resolution images). The bright spots in each FFT indicate interplanar (d) spacings of ~3.21 nm, ~3.72 nm and ~3.97 nm corresponding to the crystalline planes (012), (101) and (003), respectively. These values are consistent with those d-values expected for rhombohedral bismuth, confirming the monophase structure and high crystallinity of the BiNCs. This is supported by X-ray diffraction (XRD), Fig. 3h. The XRD peaks from the BiNCs sample align closely with reference peaks associated with the rhombohedral phase of mono-elemental bismuth (JCPDS, PDF-851329).[18,19,30,31]

The peak intensities resemble the expected relative intensities of the reference pattern, with minor deviations (Fig. 3h). The differences in peak intensities can be attributed to the growth of the BiNCs with a preferential orientation along specific crystallographic planes. The enhanced intensity of the (012) reflection suggests a higher degree of crystallographic alignment along this plane, consistent with the nanoscale dimensions and surface-dominated characteristics of the synthesized BiNCs. Additionally, slight variations in relative intensities of other reflections, such as (003) and (101), can be attributed to the different morphology and size distribution of the nanocrystals, which influence their diffraction patterns. The appearance of double peaks, instead of single peaks, may result from the Cu Kα1/Kα2 source X-ray splitting due to spin–orbit coupling,[33] a common feature reported for large single crystals where the XRD peak widths are relatively narrow and can be easily resolved. The observation of these sharp and dis-

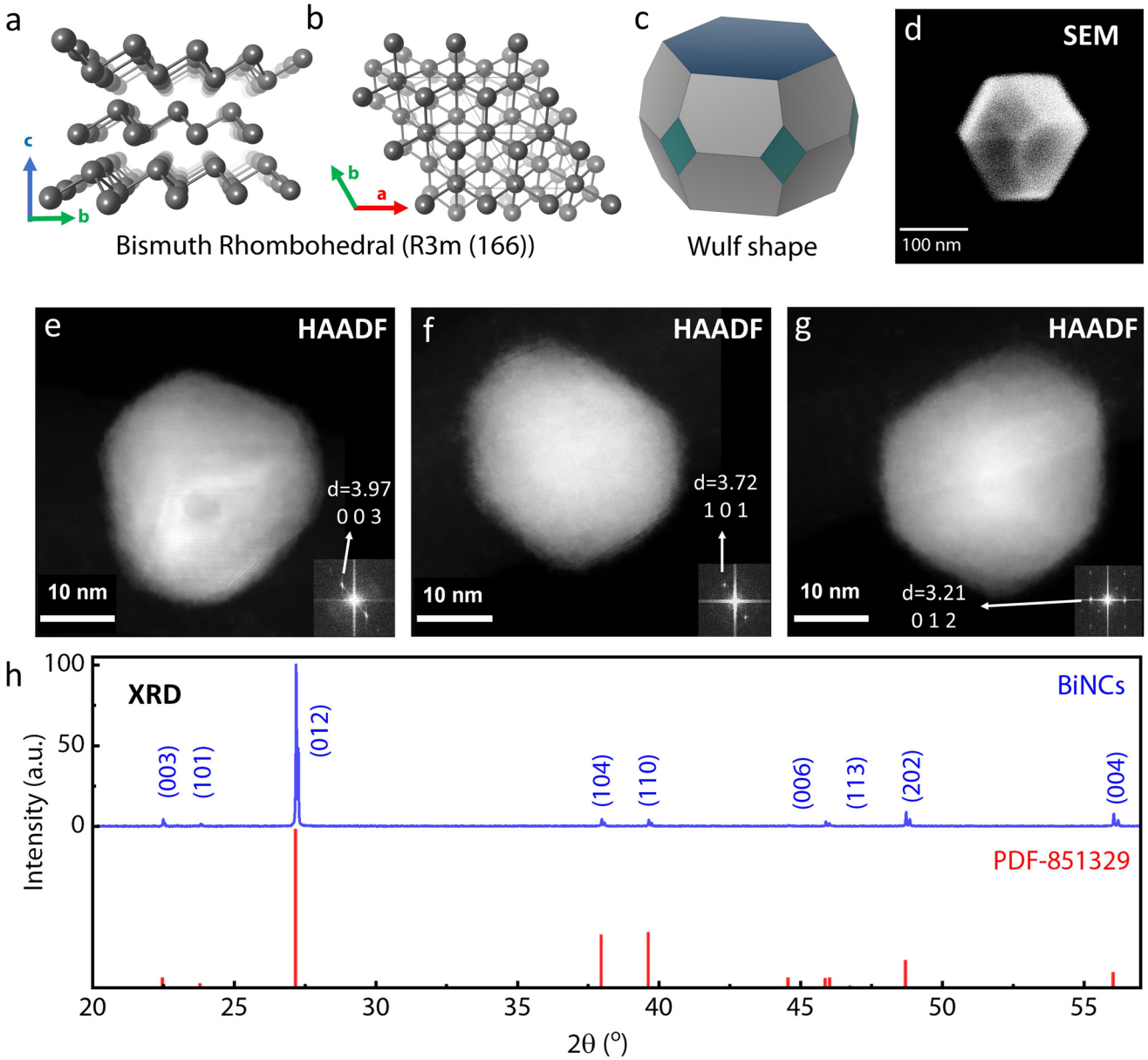

Fig. 3 Characterization of monophase, faceted BiNCs synthesized at 3.5 W. (a) and (b) Rhombohedral ($R\bar{3}m$ (166)) crystal structure of elemental Bi viewed down the *a* and *c* axes, respectively. Structures generated using VESTA.[32] (c) Expected Wulf shape (equilibrium shape) of rhombohedral Bi. (d) SE SEM image of faceted BiNCs; image acquired at 5 kV. (e)–(g) HAADF-STEM images of individual BiNCs with corresponding FFTs as insets, confirming the Rhombohedral phase of BiNCs. (h) XRD pattern of BiNCs (blue) and reference JCPDS, PDF-851329 (red), confirming their monophase nature.

tinct XRD peaks further confirms the high degree of crystallinity and monophase structure of the BiNCs.

STEM energy-dispersive X-ray spectroscopy (STEM-EDX) revealed the elemental composition of the BiNCs, Fig. 4a. The qualitative elemental maps highlight the presence of bismuth (Bi) in red, with minimal oxygen (O) content, in green. Fig. 4b presents an HAADF image of an individual BiNC overlayed with the elemental maps for Bi (M line) and O (K line). STEM-EDX line profiles (Fig. 4c) display a significantly stronger signal for Bi (M line) compared to O (K line). The extremely low and uniform oxygen signal across the crystal and grid (Fig. 4d: vacuum – A1, carbon support – A2, and inside the BiNC – A3) suggests that any oxygen present is primarily limited to the surface and cannot be attributed at the core composition of the nanocrystals, supporting the high purity and monophase nature of the BiNCs STEM-EDX spectra (Fig. 4d) were obtained from three different areas, as shown in Fig. 4b: on the carbon support of the TEM grid (A2), in the vacuum (A1) and inside the BiNC (A3). This confirms a very low oxygen content of the BiNCs. Moreover, if oxygen were

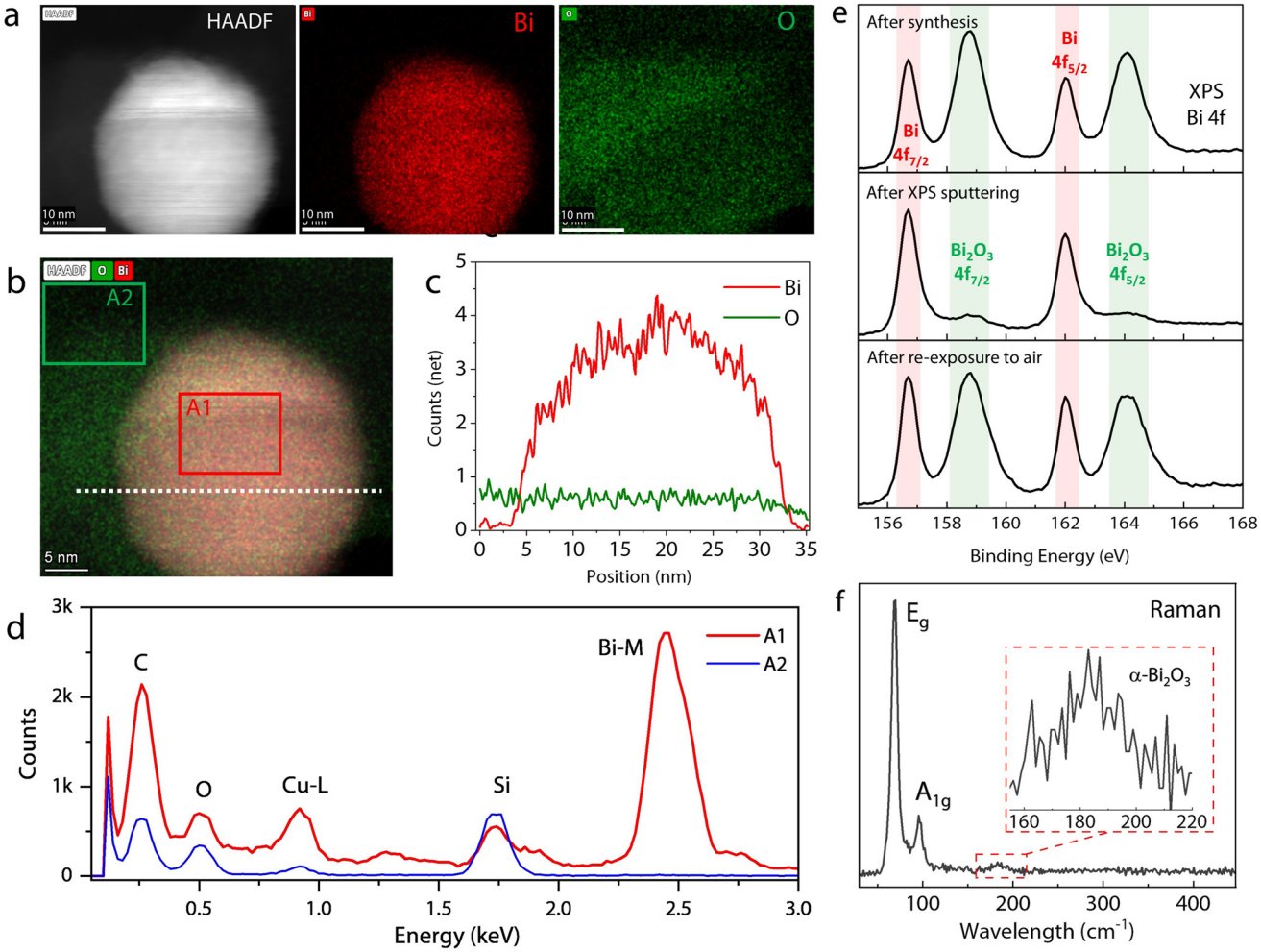

Fig. 4 Compositional analysis of BiNCs (3.5 W). (a) STEM-EDX elemental mapping of a representative BiNCs confirming a strong Bi signal (red) and minimal oxygen (green) content. (b) Overlay of HAADF image with elemental maps for Bi (M line) and O (K line) confirming spatial distribution. (c) STEM-EDX line profile across a single BiNC revealing a higher signal for Bi (M line) relative to oxygen. (d) EDX spectra from three distinct regions: the hole in the TEM grid (A1), the carbon support film (A2), and within the BiNC (A3). (e) XPS spectra of the high-resolution regions for Bi 4f: after synthesis (top spectrum), after XPS sputtering (middle spectrum), and after re-exposure to air (bottom spectrum), confirming surface oxidation upon ambient exposure after synthesis. (f) Raman spectrum showing characteristic peaks that correspond to the modes of Rhombohedral bismuth, the low-intensity peak indicates the presence of a thin native oxide formation on the surface.

incorporated into the core of BiNCs, it would cause a noticeable deviation in the fit of the crystallographic structure. However, as shown in Fig. 3, the XRD and STEM analyses confirm that this is not the case. X-ray photoemission spectroscopy (XPS) was conducted to examine the surface composition and potential oxidation of the BiNCs. We closely monitored the time the BiNCs were exposed to ambient air, approximately 4 minutes, during the transfer of the sample from the nitrogen-filled synthesis chamber to the XPS load chamber under vacuum. Fig. 4e displays the high-resolution XPS spectrum of the regions for Bi 4f for the BiNCs sample immediately after synthesis (top spectrum). The two peaks separated by 5.3 eV at binding energies of 156.7 eV and 162 eV correspond to the 7/2 and 5/2 spin–orbit components of elemental Bi. In contrast, the peaks observed at 158.7 eV and 164 eV are typically associated with Bi bonded to oxygen in the α-Bi_2O_3 phase. To confirm that this oxide layer forms after synthesis due to brief air exposure during sample transfer, we performed sputter cleaning on the sample using a monoatomic 2 keV Ar^+ gun in an ultra-high vacuum for 45 seconds to remove the surface bismuth oxide. The XPS spectrum taken after sputtering (Fig. 4e, middle spectrum) shows a significant reduction in the oxide-related peaks, indicating that the oxidation was confined to the surface of the sample. After the sample was re-exposed to air for another 4 minutes, a subsequent XPS analysis was performed. The spectrum (Fig. 4e, bottom spectrum) displays the reappearance of the oxide peaks, consistent with the initial post-synthesis measurement, confirming rapid surface oxidation post-synthesis, upon short exposure to air (~4 min).

Raman spectroscopy (Fig. 4f) further validated the rhombohedral phase of BiNCs, as indicated by two clear peaks centered at 69 cm^{-1} and 94 cm^{-1}, assigned to the E_g and A_{1g} phonon modes, respectively, in agreement with pure metallic BiNCs.[9,18,30] In addition to the crystallinity and phase, the Raman spectrum shows impurities as well as the incorporation of oxygen in BiNCs. The low-intensity peak related to a Bi_2O_3 phase at 188 cm^{-1} highlights limited surface oxidation.[9,10,34] Notably, using higher laser intensities or longer integration times during Raman spectroscopy can induce oxidation and phase transitions in BiNCs, as reported in the literature.[30,34,35]

3.3. Proposed mechanism for BiNCs formation

The formation mechanism of nanocrystal in a non-equilibrium, atmospheric pressure, plasma environment is a complex and relatively unexplored process that significantly differs from the more established low-pressure plasma sputtering techniques. In low-pressure systems, the removal of metal atoms from a solid target typically occurs through physical bombardment by energetic ions, leading to the formation of nanostructures.[36] In atmospheric pressure plasmas, the dynamics of plasma–surface interactions differ significantly, and the underlying mechanisms governing nanocrystal formation are less well understood. Although heating from the plasma gas is possible and likely occurring, other mechanisms such as ion bombardment or surface interactions from metastable or hydrogen radicals can effectively release substantial energy to the surface. The formation of the bulge is indicative of significant surface melting through all these heating processes, which seem to be crucial for the formation of BiNCs on the wire surface. The nanocrystals form directly on the molten surface of the wire, where they condense and crystallize. These localized processes at the wire surface suggest that the formation of BiNCs is driven by surface phenomena rather than by gas-phase nucleation.[37] At lower absorbed powers, no wire deformation is observed due to melting. As the power increases to around 3.5 W, the wire tip is deformed and surface melting is apparent, leading to the formation of BiNCs. Faceted structures, principally observed at 3.5 W, are a result of controlled crystal growth. However, at higher powers, closer to 4.7 W, the nanocrystals become more spherical with a substantial deformation of the wire, which indicates extensive melting beyond the surface tip.[13,20]

The formation of monophase BiNCs in the atmospheric pressure plasma environment, as opposed to multiphase structures, can be attributed to the wire temperature and the presence of hydrogen in the process gas. While the synthesis of Bi nanoparticles has been achieved also without hydrogen, we have not observed monophase or faceted BiNCs when hydrogen was not used. Hydrogen radicals and ions dissociated and ionized in the gas-phase plasma can impact the plasma–surface interactions. These factors might play a significant role in stabilizing a single crystal phase during the nucleation and growth processes. Atomic hydrogen in the plasma for instance can dissolve in the molten surface and transfer heat to the melt through exothermic recombination reactions, enhancing vaporization and particle formation. This was observed for instance also when a similar plasma was in contact with a gold wire.[37] hydrogen atoms dissolve into the molten gold wire, and their exothermic recombination reactions enhance the etching of the gold surface. This etching process results in the formation of Au vapor, which condenses to form nanoparticles.[37] A similar mechanism has been also observed in Sn–Ag nanoparticle formation.[38,39] Atomic hydrogen is found to dissolve in the molten metal surface and contribute to the formation of metal hydrides. These hydrides play a critical role in enhancing the vaporization rate of specific metals, such as Sn. The recombination of hydrogen atoms within the molten metal not only facilitates the formation of hydrides but also transfers additional heat to the melt, thereby accelerating vaporization. Our results suggest the non-equilibrium plasma environment provides a unique set of conditions for crystal growth. This balance ensures that once the initial nuclei of BiNCs form, they grow into larger crystals with a consistent phase, rather than transitioning into multiple phases as might occur in less controlled environments.

4. Conclusions

In this study, we demonstrated a gas-phase atmospheric pressure plasma synthesis method for the synthesis of high purity, monophase BiNCs. Our process is fully electrified and therefore compatible with renewable energy sources and effectively eliminates the need for complex vacuum systems and metal–organic precursors typically required in other synthesis methods. The use of process gases (*e.g.* helium) can be made sustainable through a closed-loop recycling system, given that no gaseous by-products are generated. Furthermore, as the synthesis utilizes solid bismuth metal without the need of other chemical precursors and without generating chemical waste or harmful by-products, the synthesis features characteristics aligned with a sustainable and environmentally friendly process. The control of absorbed power and incorporation of hydrogen into the process gas were key factors in promoting localized melting and surface nucleation, leading to the formation of BiNCs with a rhombohedral crystal phase. Electron microscopy techniques, XRD and Raman spectroscopy confirmed the high purity rhombohedral phase of BiNCs. Also, XPS and EDX confirmed predominantly elemental bismuth composition of the BiNCs, with minimal oxygen contribution originating from the top surface of BiNCs because of native oxide formation after synthesis. Our work provides new scientific insight into the plasma-assisted growth mechanisms of metal nanocrystals under atmospheric conditions. The ability to control crystallinity and morphology through plasma parameters is an important research aspect and our findings contribute to a broader understanding of plasma assisted nanomaterial synthesis and open new pathways for designing sustainable nanomanufacturing processes for functional materials.

Conflicts of interest

The authors declare that they have no competing interests.

Data availability

This paper is accompanied by representative samples of experimental data and the relevant numerical tabulated raw data is available from the University of Strathclyde's Research Portal at https://doi.org/10.15129/64cb56ea-6979-48d4-a45d-b1c59117921c. Detailed procedures explaining how these representative samples were selected, and how these experiments can be repeated, are provided in the corresponding sections of this paper.

Supplementary information (SI) is available. See DOI: https://doi.org/10.1039/d5nr03611a.

Additional results and raw data underlying this work are available in the SI or on request following instructions provided at [insert DOI].

Acknowledgements

This work was supported by EPSRC award no. EP/V055232/1.

References

1 Q. Yu and Y. Yang, *ChemNanoMat*, 2020, **6**, 1683–1711.
2 B. Chen, Q. Yun, Y. Ge, L. Li and H. Zhang, *Acc. Mater. Res.*, 2023, **4**, 359–372.
3 W. Huang, J. Zhu, M. Wang, L. Hu, Y. Tang, Y. Shu, Z. Xie, H. Zhang, W. Huang, J. Zhu, M. Wang, L. Hu, Y. Tang, H. Zhang, Y. Shu and Z. Xie, *Adv. Funct. Mater.*, 2021, **31**, 2007584.
4 X. Liu, S. Zhang, S. Guo, B. Cai, S. A. Yang, F. Shan, M. Pumera and H. Zeng, *Chem. Soc. Rev.*, 2020, **49**, 263–285.
5 J. Sung Son, K. Park, M.-K. Han, C. Kang, S.-G. Park, J.-H. Kim, W. Kim, S.-J. Kim, T. Hyeon, S. Son, K. Park, T. Hyeon, M. Han, S. Kim, C. Kang, S. Park, W. Kim and J. Kim, *Angew. Chem., Int. Ed.*, 2011, **50**, 1363–1366.
6 D. Leng, T. Wang, Y. F. Li, Z. Huang, H. Wang, Y. Wan, X. Pei and J. Wang, *Inorg. Chem.*, 2021, **60**, 17258–17267.
7 D. Ma, S. Pan, M. Tan, G. He and J. Zhao, *Opt. Mater.*, 2023, **145**, 114433.
8 Y. Shu, W. Hu, Z. Liu, G. Shen, B. Xu, Z. Zhao, J. He, Y. Wang, Y. Tian and D. Yu, *Sci. Rep.*, 2016, **6**, 1–8.
9 C. Rodríguez-Fernández, K. Akius, M. Morais de Lima, A. Cantarero, J. M. van Ruitenbeek and C. Sabater, *Mater. Sci. Eng., B*, 2021, **270**, 115240.
10 O. Depablos-Rivera, A. Martínez and S. E. Rodil, *J. Alloys Compd.*, 2021, **853**, 157245.
11 G. Guenther, R. Theissmann and O. Guillon, *J. Phys. Chem. C*, 2014, **118**, 27020–27027.
12 D. Lu, S. Luo, S. Liu, H. Yao, X. Ren, W. Zhou, D. Tang, X. Qi and J. Zhong, *J. Phys. Chem. C*, 2018, **122**, 24459–24466.
13 L. Ma, Y. Tian, C. Yang, Y. Li, Z. Zhou, Y. Liang, X. Tian and Y. Wang, *CrystEngComm*, 2015, **17**, 7056–7062.
14 S. Wu, Y. Jiang, L. Hu, J. Sun, P. Wan and L. Sun, *Nanoscale*, 2016, **8**, 12282–12288.
15 Z. Wei, C. Dubceac, M. A. Petrukhina and E. V. Dikarev, *Chem. Commun.*, 2019, **55**, 5717–5719.
16 H. Yang, J. Li, X. Lu, G. Xi and Y. Yan, *Mater. Res. Bull.*, 2013, **48**, 4718–4722.
17 H. Zhao, X. Sun, Z. Zhu, W. Zhong, D. Song, W. Lu and L. Tao, *J. Semicond.*, 2020, **41**, 081001.
18 Q. Zhou, D. Lu, H. Tang, S. Luo, Z. Li, H. Li, X. Qi and J. Zhong, *ACS Appl. Electron. Mater.*, 2020, **2**, 1254–1262.
19 X. Qin, C. Sui and L. Di, *Vacuum*, 2019, **166**, 316–322.
20 A. Pilidi, A. Tzanis, T. Helm, M. Arfanis, P. Falaras and T. Speliotis, *ACS Appl. Nano Mater.*, 2020, **3**, 9669–9678.
21 Z. Yang, Z. Wu, Y. Lyu and J. Hao, *InfoMat*, 2019, **1**, 98–107.
22 T. Chen, F. Meng, Z. Zhang, J. Liang, Y. Hu, W. Kong, X. L. Zhang and Z. Jin, *Nano Energy*, 2020, **76**, 105068.
23 F. He, E. S. Walker, Y. Zhou, R. D. Montano, S. R. Bank and Y. Wang, *Appl. Phys. Lett.*, 2020, **117**, 73103.
24 P. Brunet, R. J. McGlynn, B. Alessi, F. Smail, A. Boies, P. Maguire and D. Mariotti, *Nanoscale Adv.*, 2021, **3**, 781–788.
25 R. McGlynn, P. Brunet, S. Chakrabarti, A. Ganguly, H. Moghaieb, Z. Bo, P. Maguire and D. Mariotti, *Small Methods*, 2024, **8**, 2300710.
26 A. ul Haq, M. Buerkle, B. Alessi, V. Svrcek, P. Maguire and D. Mariotti, *Nanoscale Horiz.*, 2024, **9**, 2042–2050.
27 A. U. Haq, S. Askari, A. McLister, S. Rawlinson, J. Davis, S. Chakrabarti, V. Svrcek, P. Maguire, P. Papakonstantinou and D. Mariotti, *Nat. Commun.*, 2019, **10**, 817.
28 P. Cucka and C. S. Barrett, *Acta Crystallogr.*, 1962, **15**, 865–872.
29 I. D. R. Mackinnon and F. J. M. Rietmeijer, *Nature*, 1984, **311**, 135–138.
30 Y. Hu, J. Liang, Y. Gu, S. Yang, W. Zhang, Z. Tie, J. Ma and Z. Jin, *Nano Lett.*, 2023, **23**, 10512–10521.
31 C. Dolle, V. Oestreicher, A. M. Ruiz, M. Kohring, F. Garnes-Portolés, M. Wu, G. Sánchez-Santolino, A. Seijas-Da Silva, M. Alcaraz, Y. M. Eggeler, E. Spiecker, J. Canet-Ferrer, A. Leyva-Pérez, H. B. Weber, M. Varela, J. J. Baldoví and G. Abellán, *J. Am. Chem. Soc.*, 2023, **145**, 12487–12498.
32 K. Momma and F. Izumi, *J. Appl. Crystallogr.*, 2011, **44**, 1272–1276.
33 N. Stojilovic, *J. Chem. Educ.*, 2018, **95**, 598–600.
34 R. A. Lewis and J. A. Steele, *Opt. Mater. Express*, 2014, **4**, 2133–2142.

35 M. A. Zepeda, M. Picquart and E. Haro-Poniatowski, *MRS Proc.*, 2012, **1477**, 28–33.
36 J. T. Gudmundsson, *Plasma Sources Sci. Technol.*, 2020, **29**, 113001.
37 Y. Shimizu, *AIP Adv.*, 2017, **7**, 15316.
38 M. Tanaka and T. Watanabe, *Thin Solid Films*, 2008, **516**, 6645–6649.
39 M. Tanaka and T. Watanabe, *Jpn. J. Appl. Phys.*, 2013, **52**, 076201.